

Numerical simulation of the Tayler instability in liquid metals

This content has been downloaded from IOPscience. Please scroll down to see the full text.

2013 New J. Phys. 15 043034

(<http://iopscience.iop.org/1367-2630/15/4/043034>)

View [the table of contents for this issue](#), or go to the [journal homepage](#) for more

Download details:

IP Address: 128.138.138.122

This content was downloaded on 09/02/2015 at 22:30

Please note that [terms and conditions apply](#).

Numerical simulation of the Tayler instability in liquid metals

Norbert Weber¹, Vladimir Galindo, Frank Stefani, Tom Weier and Thomas Wondrak

Helmholtz-Zentrum Dresden-Rossendorf, PO Box 510119, D-01314 Dresden, Germany

E-mail: Norbert.Weber@hzdr.de

New Journal of Physics **15** (2013) 043034 (19pp)

Received 13 December 2012

Published 19 April 2013

Online at <http://www.njp.org/>

doi:10.1088/1367-2630/15/4/043034

Abstract. The electrical current through an incompressible, viscous and resistive liquid conductor produces an azimuthal magnetic field that becomes unstable when the corresponding Hartmann number exceeds a critical value of the order of 20. This Tayler instability (TI), which is not only discussed as a key ingredient of a nonlinear stellar dynamo model (Tayler–Spruit dynamo), but also as a limiting factor for the maximum size of large liquid metal batteries, was recently observed experimentally in a column of a liquid metal (Seilmayer *et al* 2012 *Phys. Rev. Lett.* **108** 244501). On the basis of an integro-differential equation approach, we have developed a fully three-dimensional numerical code, and have utilized it for the simulation of the Tayler instability at typical viscosities and resistivities of liquid metals. The resulting growth rates are in good agreement with the experimental data. We illustrate the capabilities of the code for the detailed simulation of liquid metal battery problems in realistic geometries.

¹ Author to whom any correspondence should be addressed.



Content from this work may be used under the terms of the [Creative Commons Attribution 3.0 licence](https://creativecommons.org/licenses/by/3.0/). Any further distribution of this work must maintain attribution to the author(s) and the title of the work, journal citation and DOI.

Contents

1. Introduction	2
2. Mathematical model	5
3. Numerical scheme and convergence	7
3.1. Grid refinement	8
3.2. Alfvén–Courant number and time steps	9
4. Results for a cuboid geometry	10
4.1. Shape, alignment and chiral symmetry breaking	11
4.2. Saturation levels of the Tayler instability	13
4.3. Critical current as a function of the aspect ratio	13
5. Validation of experimental results	15
6. Conclusion and outlook	17
Acknowledgments	18
References	18

1. Introduction

Current-driven instabilities have been known in plasma physics for many decades [2]. A paradigm for their occurrence is the z -pinch, a cylindrical plasma column with an electrical current in the direction of the cylinder axis that produces an azimuthal magnetic field. Recently, Bergerson *et al* [3] have evidenced the onset of kink-type instabilities in a line-tied screw pinch when the ratio of the axial to the azimuthal magnetic field (the safety parameter) drops below a certain critical value.

For a purely azimuthal magnetic field, the onset of current-driven instabilities depends basically on the detailed radial dependence $B_\varphi(r)$. For the kink-type instability (azimuthal wavenumber $m = 1$), the relevant criterion is

$$\frac{\partial(rB_\varphi^2(r))}{\partial r} > 0, \quad (1)$$

which had been derived by Vandakurov [4] and Tayler [5]. Strictly speaking, this condition holds only when not taking into account the stabilizing role of rotation, viscosity, resistivity or density stratification. Focusing on the latter, the term *Tayler instability* had been coined by Spruit [6] to describe a situation in which the azimuthal magnetic field becomes strong enough to act against the stable stratification in a star. This instability is quite remarkable, since it could provide the second ingredient, in addition to differential rotation, for an alternative type of stellar dynamo, which is now called the *Tayler–Spruit dynamo*. Although this sort of nonlinear dynamo is at present controversially discussed and might fail to work under realistic conditions [7], the underlying kink instability could have important astrophysical consequences, in particular for the extreme spin down of the cores of white dwarfs [8], for chemical mixing in stars [9] or for the occurrence of helical structures in cosmic jets [10].

Resistivity and viscosity have a similar stabilizing effect on kink instability as density stratification. By slightly stretching the original semantics [6], we will use here the term Tayler instability (TI) for this viscous and resistive case too, keeping in mind that in either case the azimuthal magnetic field has to exceed a certain critical value in order to become unstable.

In plasma physics the effect of viscosity and resistivity has been studied for various boundary conditions and profiles of the electrical current [11, 12]. Apart from details, it was shown that the onset of TI occurs only when the product of the Lundquist number $S = \mu_0 \sigma R v_A$ and the so-called Alfvén–Reynolds number $Re_A = \nu^{-1} R v_A$ exceeds a value of the order of 10^3 . Here, μ_0 is the magnetic permeability constant, σ and ν are the conductivity and the viscosity of the fluid, R is the radius of the pinch and $v_A := B(\mu_0 \rho)^{-1/2}$ is the Alfvén speed which is proportional to the magnetic field B (ρ is the density of the fluid).

Going over from plasma physics, with all its peculiarities due to compressibility, anisotropic viscosities and conductivities, as well as complicated boundary conditions, to the paradigmatic case of an incompressible, viscous and resistive cylindrical fluid with a homogeneous current distribution, Rüdiger *et al* [13] were able to show that the key parameter is the Hartmann number, $Ha = BR(\sigma/\rho\nu)^{1/2}$, which should exceed a value of approximately 25 for the TI to set in when we take $B = B_\phi(R)$. This is completely consistent with the former results in plasma physics because $Ha^2 = S Re_A$. With typical viscosities and conductivities of liquid metals, the critical electrical current is of the order of 10^3 A. Using the eutectic alloy GaInSn, we had experimentally confirmed the onset of TI at a critical current of approximately 2.7 kA, as well as the numerically predicted increase of this threshold when insulating inner cylinders were inserted into the liquid metal.

Interestingly, currents of this order would indeed be relevant for large-scale liquid metal batteries which are at present strongly discussed as a cheap means for the storage of highly intermittent renewable energies [14, 15]. Smaller versions of these devices were already studied in the 1960s [16, 17]. Basically, liquid metal batteries consist of a self-assembling stratified system of a heavy liquid metal or metalloid (e.g. Bi, Sb) at the bottom, an appropriate molten salt mixture as electrolyte in the middle and a light alkaline or earth alkaline metal (e.g. Na, Mg) at the top (see figure 1). Choosing Na and Bi as an example, Na will lose one electron during the discharge process, turning into Na^+ . This ion diffuses through the electrolyte into the lower Bi layer where it is reduced and alloys with Bi to NaBi. Thus, the lower part of the battery will increase in size during discharge and the volume of the upper part will decrease correspondingly.

While small versions of such batteries have already been tested [15], the occurrence of the TI could represent a serious problem for the integrity of the stratification in larger batteries [18]. This is all the more an issue as the highly resistive electrolyte should be chosen as thin as possible in order to maintain a reasonable cell voltage. In [18], we had proposed a simple trick to suppress the TI in liquid metal batteries by just returning the battery current through a bore in the middle. By the resulting change of the radial dependence of $B_\phi(r)$ it is possible to prevent the (ideal) condition (1) for the onset of the TI.

In spite of such attempts to suppress the TI, it is worthwhile to study in detail the flow structure that would arise from it, and the resulting consequences for the stratification of the three-layer system. A first step in this direction is the determination of the final velocity field in the saturated state of the TI in a single metallic phase. The code utilized up to now for the simulation of the liquid metal experiment was well capable of determining the critical current and the growth rates for the onset of the TI [19], but the resulting scale of the velocity in the saturated state was less secure. This has to do with the fact that liquid metals are characterized by a very small magnetic Prandtl number $Pm := \nu \mu_0 \sigma \sim 10^{-6} - 10^{-5}$. The usual numerical schemes for the simulation of TI, which solve the Navier–Stokes equation (NSE) for velocity and the induction equation for magnetic field, only typically work for values

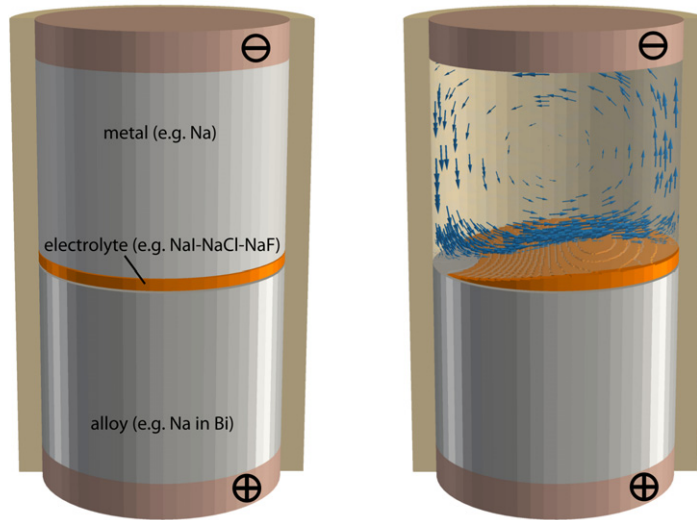


Figure 1. Sketch of a liquid metal battery with typical inventory (left). The electrolyte works as an ion conductor and separates the two liquid metals. A movement of the fluid may wipe the electrolyte and lead to an internal short circuit and thereby a battery failure (right). The TI will induce one or several convection cells in the conducting liquid metal layers.

of Pm down to 10^{-2} . Applying the code at these much too high Pm and scaling the resulting velocity level by v/R , one arrives at velocity scales of the order of mm s^{-1} . However, an extrapolation over four orders of magnitude is somewhat risky, and definitely needs justification by codes that can cope up with realistic values of Pm .

In this paper, we circumvent the Pm limitations of those codes that rely on the differential equation approach. We do this by replacing the solution of the induction equation for the magnetic field by applying the so-called quasistatic approximation [20]. This approximation means that we skip the explicit time dependence of the magnetic field by computing the electrostatic potential by a Poisson equation and then deriving the electric current density. However, in contrast to many other applications in which this procedure is sufficient, in our case we cannot avoid computing the induced magnetic field, too. The reason for that is the existence of an externally applied current in the fluid. Computing the Lorentz force term it turns out that the product of the applied current times the induced field is of the same order as the product of the magnetic field (due to the applied current) times the induced current. Here, we compute the induced magnetic field from the induced current density by means of the Biot–Savart law. This way, we arrive at an integro-differential equation approach, as had already been used by Meir *et al* [21].

In the following, we will describe the mathematical basis of the integro-differential equation approach in the quasistatic approximation. Then, we will present the developed numerical model that utilizes the open source CFD library OpenFOAM® [22], supplemented with an message passing interface (MPI)-parallelized implementation of the Biot–Savart law. We will discuss, in particular, the convergence properties of this numerical scheme when applied to a TI problem in cuboid geometry. Based on this, we will study the effect of a varying geometric aspect ratio on the spatial structure of the TI and on the critical current. We will also discuss the effect of spontaneous chiral symmetry breaking as was recently discussed by

Gellert *et al* [23] and Bonanno *et al* [24]. Then, we will apply our model to the cylindrical TI experiment [1], for which we will show a surprising agreement between measured and computed growth rates. The paper closes with a discussion of the results, with an outlook toward more detailed simulations of liquid metal batteries, and with prospects for a larger TI-related experiment.

2. Mathematical model

The initial point for describing fluid dynamics in a liquid metal is the NSE

$$\dot{\mathbf{v}} + (\mathbf{v} \cdot \nabla) \mathbf{v} = -\frac{\nabla p}{\rho} + \nu \Delta \mathbf{v} + \frac{\mathbf{f}}{\rho} \quad (2)$$

with \mathbf{v} denoting the velocity, p the pressure, ρ the density, ν the kinematic viscosity and \mathbf{f} the body force density. For incompressible fluids, the continuity equation $\nabla \cdot \mathbf{v} = 0$ has to be taken into account.

The trigger of the TI is the Lorentz force

$$\mathbf{f} = \mathbf{f}_L = \mathbf{J} \times \mathbf{B} \quad (3)$$

with \mathbf{J} meaning the current density. Note that the magnetic field \mathbf{B} consists of two parts: the static field \mathbf{B}_0 , generated by the applied current I (or the corresponding current density \mathbf{J}_0), and the induced magnetic field \mathbf{b} , generated by the motion of the electrically conducting fluid. Although in our problem \mathbf{b} is rather small, it must not be neglected in the expression for the Lorentz force because it is multiplied with the large current density \mathbf{J}_0 .

The usual way of simulating the magnetic field evolution is by solving the induction equation

$$\dot{\mathbf{B}} + (\mathbf{v} \cdot \nabla) \mathbf{B} = (\mathbf{B} \cdot \nabla) \mathbf{v} + \frac{1}{\mu_0 \sigma} \Delta \mathbf{B}. \quad (4)$$

The solution of this equation requires suitable boundary conditions for the magnetic field, which can be implemented either by solving a Laplace equation in the exterior of the fluid [25, 26] or by equivalent boundary element methods [27–29].

In the following, we choose a second option, i.e. we compute the magnetic field using the Biot–Savart law,

$$\mathbf{B}(\mathbf{r}) = \frac{\mu_0}{4\pi} \int dV' \frac{\mathbf{J}(\mathbf{r}') \times (\mathbf{r} - \mathbf{r}')}{|\mathbf{r} - \mathbf{r}'|^3} \quad (5)$$

which is the inversion of Ampère's law $\nabla \times \mathbf{B} = \mu_0 \mathbf{J}$. Here \mathbf{r} means the point coordinate where \mathbf{B} has to be computed, and \mathbf{r}' is the integration coordinate, which runs through the whole domain where \mathbf{J} exists.

This way, the problem is shifted from the determination of the magnetic field \mathbf{B} to the determination of the current density \mathbf{J} . The approach of using the Biot–Savart law was proposed and utilized by Meir *et al* [21] and will be adopted for our case.

The flowchart of the numerical model is shown in figure 2. Assuming the current I through our cylindrical vessel as given (e.g. the battery charging current), we compute the corresponding current density \mathbf{J}_0 and the associated static magnetic field \mathbf{B}_0 . For an infinitely long vertical cylinder, we would obtain

$$\mathbf{B}_0(x, y) = \frac{\mu_0 J_0}{2} (y \mathbf{e}_x - x \mathbf{e}_y) \quad (6)$$

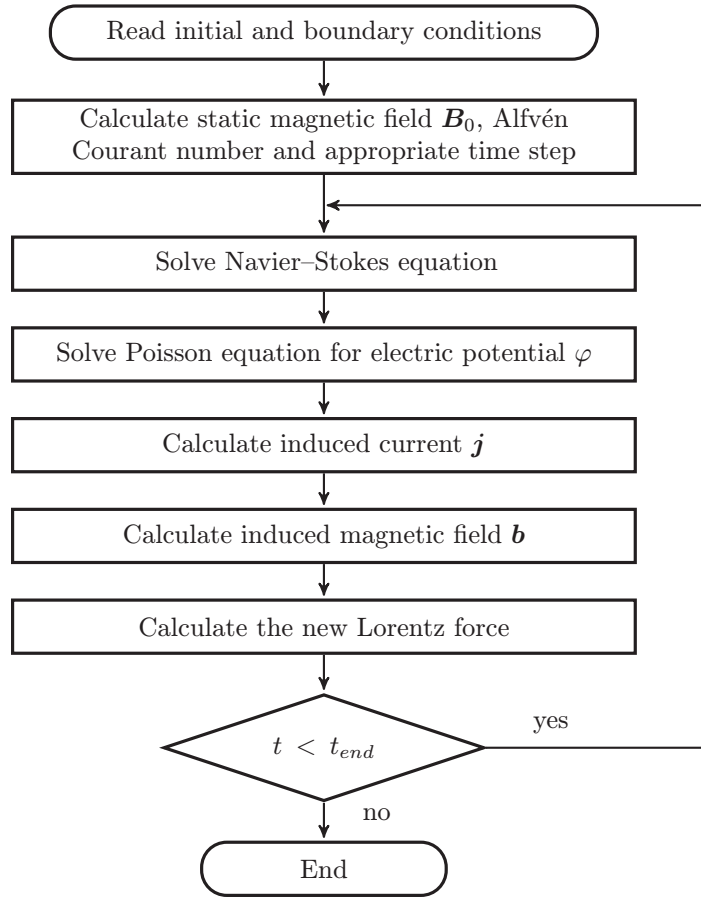


Figure 2. Flowchart of the simulation model.

in the Cartesian coordinates x, y, z . For real geometries with external leads to the system, \mathbf{B}_0 could still be computed by Biot–Savart’s law.

In the main loop of our numerical scheme, the NSE (2) is first solved, followed by a velocity corrector step to ensure continuity ($\nabla \cdot \mathbf{v} = 0$). Then we have to find the electric current density. Presupposing the magnetic Reynolds number $Rm = \mu_0 \sigma R v$ on the basis of the TI-triggered velocity scale v to be small, we can invoke the quasistatic approximation [20]. This means that we express the electric field by the gradient of an electrostatic potential, $\mathbf{E} = -\nabla \Phi$. Applying the divergence operator to Ohm’s law in moving conductors, $\mathbf{J} = \sigma(-\nabla \Phi + \mathbf{v} \times \mathbf{B})$, and demanding charge conservation, $\nabla \cdot \mathbf{J} = 0$, we arrive at the Poisson equation

$$\Delta \varphi = \nabla \cdot (\mathbf{v} \times \mathbf{B}) \quad (7)$$

for the perturbed electric potential $\varphi = \Phi - J_0 z / \sigma$, where z is the coordinate along the battery axis pointing in the direction of the applied potential difference. By subtracting the electric potential caused by the battery charging current I , we can easily set the boundary conditions at the electrodes to $\varphi = 0$. Since no current is allowed to flow through the insulating rim of the cylindrical vessel, we assume $\mathbf{n} \cdot \nabla \varphi = 0$, with \mathbf{n} being the surface normal vector.

Having derived the potential in the fluid by solving the Poisson equation, we easily recover the current density induced by the fluid motion as

$$\mathbf{j} = \sigma (-\nabla \varphi + \mathbf{v} \times \mathbf{B}) \quad (8)$$

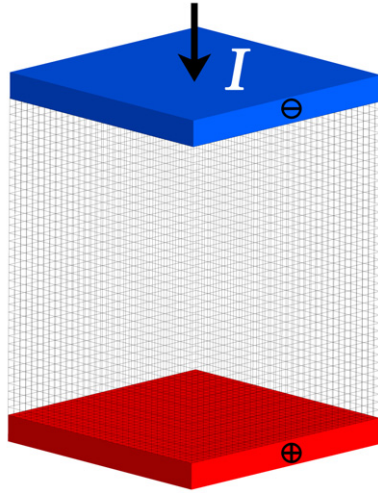


Figure 3. Geometric setting for the simulation of the TI in cuboid geometry. The electric current is assumed to be impressed by infinitely long electrodes. The NSE, enhanced by the Poisson equation and the Biot–Savart law, is solved in the gridded volume between the electrodes.

and then the induced magnetic field by using the Biot–Savart law (5). The total current density is

$$\mathbf{J} = \mathbf{j} - J_0 \mathbf{e}_z. \quad (9)$$

In a last step, the Lorentz force, to be implemented in the NSE, is calculated according to

$$\mathbf{f}_L = \mathbf{J} \times \mathbf{B} = (\sigma (-\nabla\varphi + \mathbf{v} \times (\mathbf{B}_0 + \mathbf{b})) - J_0 \mathbf{e}_z) \times (\mathbf{B}_0 + \mathbf{b}). \quad (10)$$

It should be noted again that the (small) induced magnetic field \mathbf{b} cannot be omitted here, since its product with the (large) impressed current \mathbf{J}_0 is of the same order as the product of the (small) induced current \mathbf{j} with the (large) magnetic field \mathbf{B}_0 .

Assuming an implementation of this scheme on a certain grid, one has to ask for the allowed time steps to keep the time evolution of the system stable. For this it is important to consider not only the Courant number based on the hydrodynamic velocity v , but also the Alfvén–Courant number based on the Alfvén velocity $v_A = B/(\mu_0 \rho)^{1/2}$. The influence of the Alfvén–Courant number on the accuracy of the simulations is discussed in the following section.

3. Numerical scheme and convergence

In this section, we will examine the numerical scheme with respect to its convergence and error characteristics. We will study both the variation of the grid spacing and of the time steps. We will further consider the case where different grid spacings and time steps are used for the NSE and for the Biot–Savart law. The temporal discretization scheme used for all simulations is of second order (Crank–Nicholson), while the spacial scheme is of fourth order.

In order to utilize the convenience of orthogonal cells for grid refinement, a cuboid with the dimensions of $96 \times 96 \times 120 \text{ mm}^3$ is used as a reference geometry, see figure 3.

Anticipating the later simulation of the recent TI experiment [1], we will start working here with the real material parameters of GaInSn: electric conductivity $\sigma = 3.29 \times 10^6 \text{ S m}^{-1}$, density $\rho = 6403 \text{ kg m}^{-3}$ and kinematic viscosity $\eta = 3.4 \times 10^{-7} \text{ m}^2 \text{ s}^{-1}$.

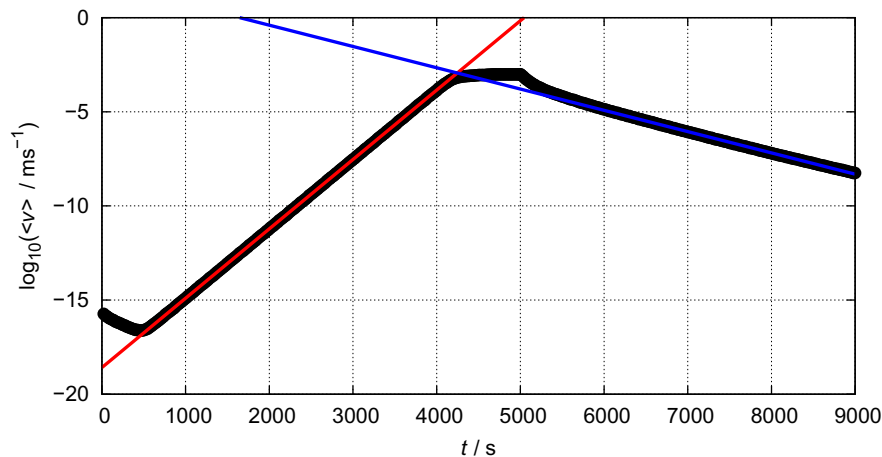


Figure 4. The typical flow development of the TI is characterized by an initial phase, an exponential growth phase and a final saturation phase ($I = 8$ kA for $t < 5000$ s). The growth rate corresponds to the slope of the red line. On switching off the current, at $t = 5000$ s, the TI decays exponentially. The decay rate corresponds to the slope of the blue line.

Figure 4 shows a typical evolution of the TI in time (here for $I = 8$ kA), comprising an initial phase where the eigenfield of the TI develops, followed by a long period (over ~ 3000 s) in which this eigenfield grows exponentially, and a final phase in which the TI saturates at a certain velocity level. Reaching saturation, we switch off the current and observe a characteristic exponential decay. The decay rate for $I = 0$ A is -0.00268 s $^{-1}$.

In the following, we will compare the growth rates, as they can be read off during the exponential growth phase for different grid spacings and time steps, with respect to their relative errors which are derived by dividing the absolute error by the difference of the TI growth rates at 10 and 0 kA.

3.1. Grid refinement

We start by exploring the effects of different grid sizes of the cubic cells with an edge length between 1 and 8 mm. Using the finite-volume method of OpenFOAM[®] for the simulation, the values from the cell centers have to be interpolated to the cell faces in order to ensure continuity. For this interpolation, we employ two different methods, a linear one and a cubic one, and compare the results in figure 5. As expected, the cubic interpolation provides better results, i.e. the growth rates are typically higher. While it would be numerically very demanding to go below a cell size of 1 mm, we expect the difference between cubic and linear interpolations to be zero in the limit of vanishing cell size. With that assumption, we perform a Richardson extrapolation to obtain the best estimated growth rate of the TI. Taking this value as a reference, the relative error of the growth rates is then calculated as a function of the grid cell size (figure 6). Although the error calculation is based on an extrapolated value, this approach is recommended by CFD best practice guidelines [30] and was carried out as described by Faires and Burden [31]. Using the values of the growth rate of the TI computed on four grids with cell sizes h , $h/2$, $h/4$ and $h/8$, respectively, we calculate the corresponding extrapolated values by following the Richardson extrapolation scheme and achieve a relative error smaller than 0.007 in the highest order.

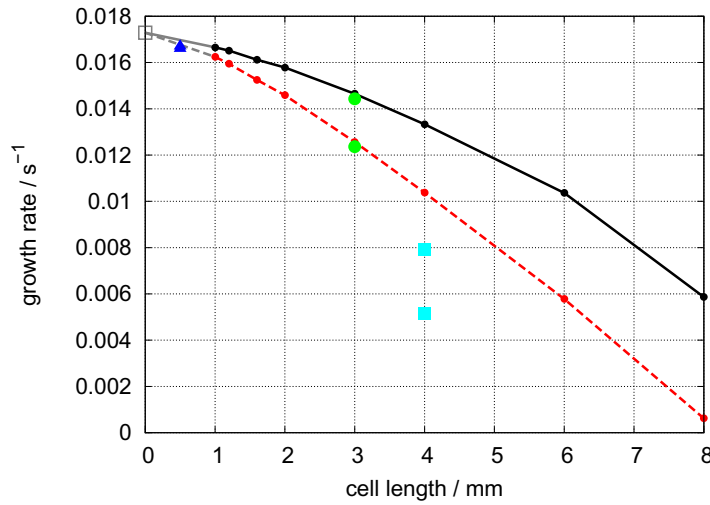


Figure 5. Influence of the grid cell size on the growth rate. Simulation is carried out for linear cell-face interpolation (red dashed line) as well as the cubic one (black line). A Richardson extrapolation yields the best estimated value of 0.0173 s^{-1} (gray). Computing the Biot–Savart law with 8 mm cells does not give good results (■), while a 6 mm grid is sufficient (●). This technique allows an additional refinement of the initial mesh, i.e. to solve the NSE on a 0.5 mm grid (▲).

Since the solution of the Biot–Savart law is numerically very costly, we have additionally checked the possibility of speeding up this part of the simulation. While the two lines in figure 5 result from computations in which the NSE and the Biot–Savart law are implemented on the same grid, the green circles and the light blue squares correspond to the cases in which the Biot–Savart law is realized on coarser grids. In contrast to the \mathbf{b} -calculation with cells of 8 mm edge length, which does not give good results (see figure 5), a grid cell size of 6 mm already seems to be sufficient. Solving the NSE on a 3 mm grid, and computing the Biot–Savart law on a 6 mm grid, provides almost the same results as doing both on a 3 mm grid. This is numerically very convenient because the Biot–Savart law needs the square of cell numbers as operations whenever carried out, i.e. a coarse grid makes the simulation much faster. The resulting slightly lower growth rates when working with two meshes appear because of the inter-grid mapping. The interpolation flattens the \mathbf{b} -field a little bit, which reduces the growth rate—but the difference is very small.

3.2. Alfvén–Courant number and time steps

As is usual, during the time integration of the NSE we have to fulfill the Courant–Friedrichs–Lewy (CFL) condition for the time step. In our special problem, however, information is not only transferred by the flow velocity, but also electromagnetically with the Alfvén velocity $v_A = B/(\mu_0 \rho)^{1/2}$, which is the only characteristic velocity in the initial state of rest. We consider this by introducing an ‘Alfvén–Courant number’ and compute the maximum time step on that basis. Due to the high currents at which TI is expected to set in, and the consequently high magnetic field B_0 , this time step has to be very short in spite of the low fluid velocities.

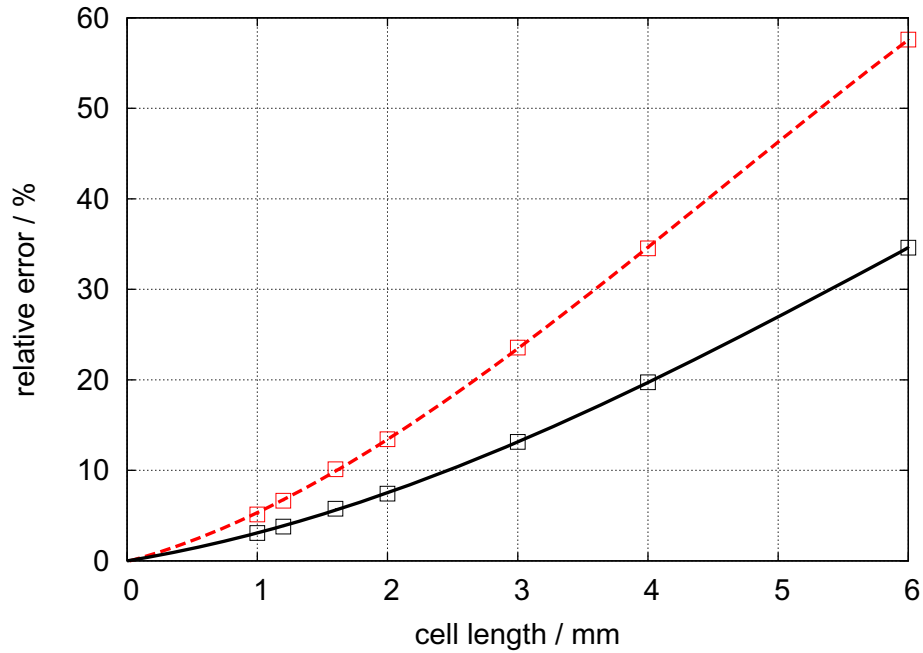


Figure 6. Influence of the grid cell size on the error of the growth rate. The growth rate at 0 mm was Richardson extrapolated and used as a reference. The black line stands for cubic cell-face interpolation and the red dotted one for linear interpolation.

Fortunately, it turns out that choosing the Alfvén–Courant number larger than one does not lead to a completely unstable system, as would be expected for a purely differential equation system. Evidently, the mixed integro-differential equation approach makes the system somewhat more ‘benign’ and less vulnerable to violations of the CFL condition. Of course, the error increases significantly with increasing the Alfvén–Courant number as shown in figure 7. Taking the average velocity in the asymptotic saturated steady state of an only slightly overcritical system (e.g. figure 4), a hydrodynamic Courant number of one would correspond to an Alfvén–Courant number of approximately 250, i.e. using the hydrodynamic CFL condition would result in an unacceptable error.

Besides calculating the magnetic field \mathbf{b} on a coarser grid than the velocity field, we have also tested to compute it only at every n th time step. Figure 8 shows that it is well possible to compute the Biot–Savart integrals only every 100th time step. The benefit in computation time is especially high when solving the NSE and the Biot–Savart law on the same grid, as the latter takes usually more than 100 times longer than solving all other equations.

4. Results for a cuboid geometry

In this section, we will focus on the characteristic eigenmode structure of the TI, on the typical velocities in the saturated regime and on the critical currents as a function of various geometry parameters. The simulations are done for a cuboid volume with a base area of $96 \times 96 \text{ mm}^2$, but with different heights.

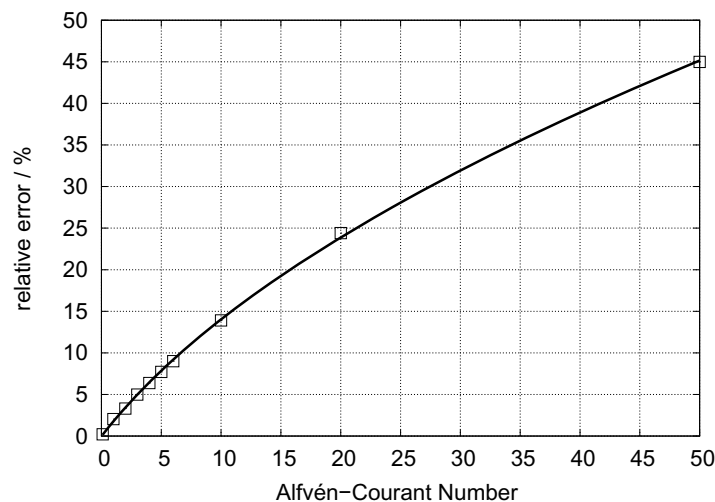


Figure 7. Influence of the Alfvén–Courant number on the error of the growth rate. The relative errors of the growth rate were computed using an extrapolated value as a reference, which corresponds to an Alfvén–Courant number of 0.

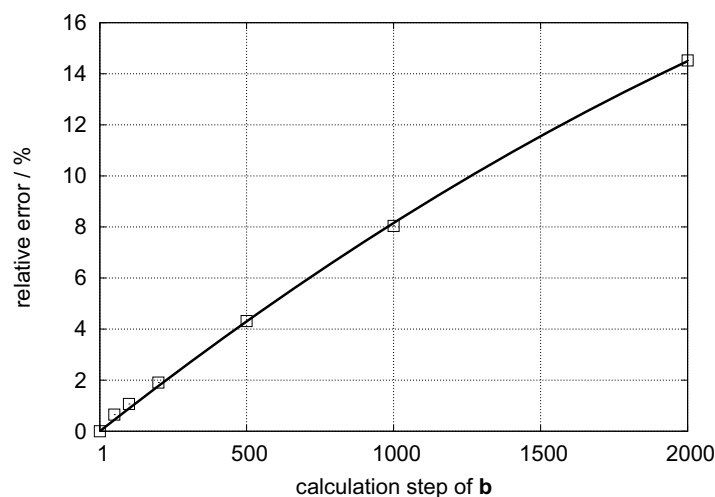


Figure 8. Error of the growth rate of the TI depending on how often the induced magnetic field \mathbf{b} is calculated. As the TI is growing slowly and therefore \mathbf{b} changes slowly, the simulation can be accelerated by not doing Biot–Savart on every time step.

4.1. Shape, alignment and chiral symmetry breaking

Basically, the TI appears in the form of convection cells that are vertically stacked one over another (see figure 9). The fluid in one cell rotates around some horizontal axis, and the sense of rotation is changing from one cell to the neighboring one. Referring, for the moment, to a cylindrical geometry, this cell structure represents a non-axisymmetric flow structure, with an azimuthal wavenumber $m = \pm 1$. Since the present simulations are carried out for a cuboid geometry, one could imagine, e.g., a preferred alignment of the convection cells with the

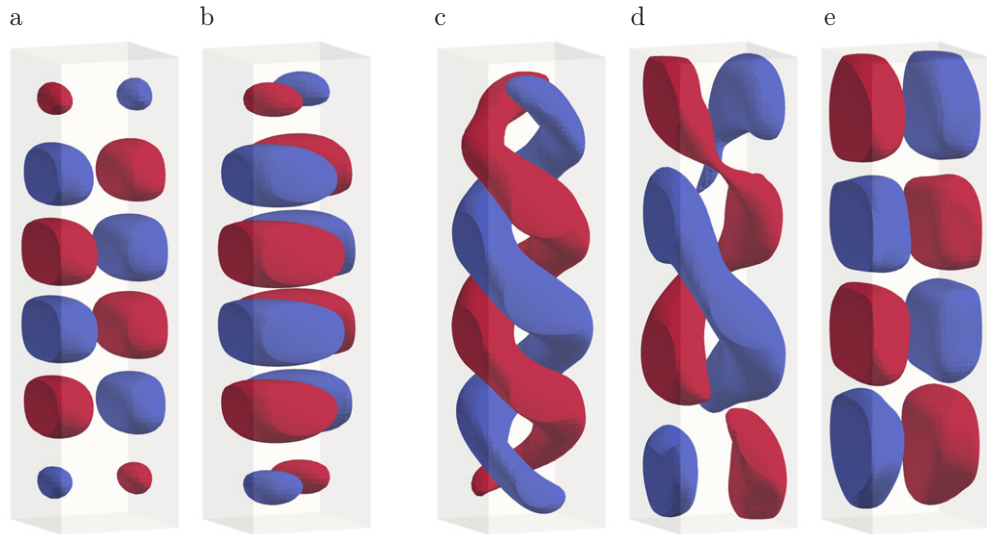


Figure 9. Iso-surface plots of the magnetic field b_z for a cuboid of $h = 360$ mm. Depending on the initial velocity conditions, the convection cells of the TI align to an arbitrary direction ((a) orthogonal and (b) diagonal to the base cube). Due to a helical perturbation, a helical TI may grow ((c) $t = 2300$ s), but almost disappears later ((d) $t = 2400$ s and (e) $t = 2800$ s). The corresponding time graph is shown in figure 10.

diagonal of the base area. However, this is, generally, not the case. In fact, the alignment of the cells depends strongly on the chosen initial conditions. Assuming a small perturbation in the x -direction, the TI will arise around the y -axis (figure 9). For arbitrary initial velocity, the TI will develop around a random axis.

Most interestingly, a transient helical shape of the TI may result under certain initial conditions (see figure 9, right). This was observed, e.g., with an initial velocity in the z -direction and, in particular, when the height of the simulated geometry did not match an integer multiple of the wavelength of the TI. The helical perturbation may develop if, e.g., two convection cells arise simultaneously, but with azimuthal twisted rotation axes. The growth rates of the non-helical and the helical TI state were found to be very similar. Figure 10 shows the velocity and the normalized mean value of the helicity $H = \mathbf{v} \cdot (\nabla \times \mathbf{v})$ of a non-helical (blue) and of a helical (red) state for a $96 \times 96 \times 360$ mm³ geometry ($h = 3.1\lambda$). Reaching a certain velocity level in the saturated regime, the helicity of the helical state decreases significantly and finally goes to zero. Approximately at the same time (at ~ 2500 s) the saturated state of the formerly non-helical state acquires also some helicity, which finally goes to zero, too. The ultimate convection cells of the two states are not equal (compare figure 9, left and right), and seem to depend on different initial conditions of the velocity.

This transient appearance of helical TI structures is quite remarkable, since it corresponds to the spontaneous chiral symmetry breaking that was recently observed by Gellert *et al* [23] and discussed in detail by Bonanno *et al* [24]. Here we can only evidence its occurrence, while a more comprehensive study of this effect is left for future studies.

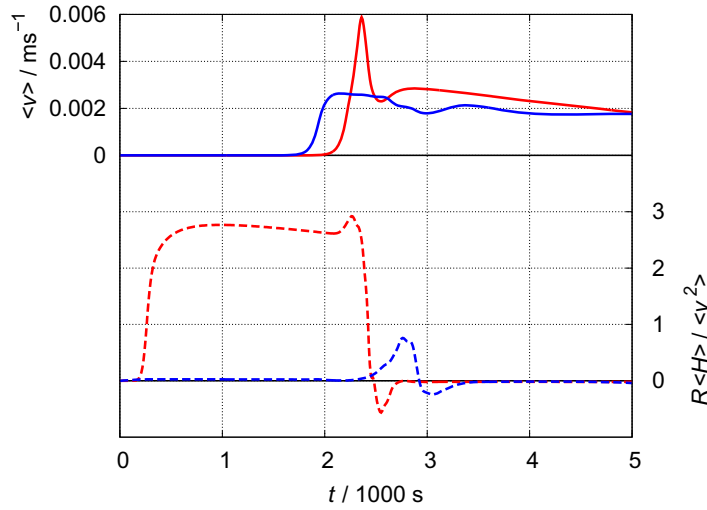


Figure 10. Temporal evolution of the mean velocity (continuous lines in the upper part) and of the corresponding normalized helicity (dotted lines in the lower part), with $H = \mathbf{v} \cdot (\nabla \times \mathbf{v})$ and R as the half side length of the base square. The height of the cuboid is 360 mm and the applied current is 10 kA. The blue lines correspond to an initial velocity along the diagonal of the base cube, while the red plots result from an initial velocity in the z -direction.

4.2. Saturation levels of the Tayler instability

To investigate the saturation level of the TI, we have carried out simulations using different currents for a cuboid geometry of $96 \times 96 \times 120 \text{ mm}^3$ and a grid cell length of 3 mm. When the critical current for the onset of the TI is exceeded, any small disturbance can initiate the instability, which then needs some time to establish its eigenmode. Thereafter, this eigenmode grows exponentially, see figure 11. For currents only slightly above the critical one, the instability grows very slowly. In such a case, it may take tens of minutes until the TI reaches its saturated final state. Figure 12 shows the dependence of the final velocities on the applied current. We see that the maximum velocities grow from a few mm s^{-1} close to the critical current, to nearly 14 cm s^{-1} at 50 kA. Velocities on this scale would clearly be problematic for the stability of the layer stratification in liquid metal batteries.

4.3. Critical current as a function of the aspect ratio

To investigate the dependence of the critical current on the aspect ratio of the fluid volume, we consider a cuboid with a base area of $96 \times 96 \text{ mm}^2$ that is changed in height from 24 to 480 mm.

As a first estimate of the critical wavelength of the TI, we can take the value for an infinitely long cylinder of radius R ,

$$\lambda = 2\pi R/k \quad (11)$$

for which the critical wavenumber k is known to be 2.47 [19]. Embedding this cylinder in the cuboid to be considered here, the resulting wavelength would be $\lambda = 122 \text{ mm}$. To obtain the corresponding true spatial wavelength for the cuboid geometry, the TI is simulated for a very

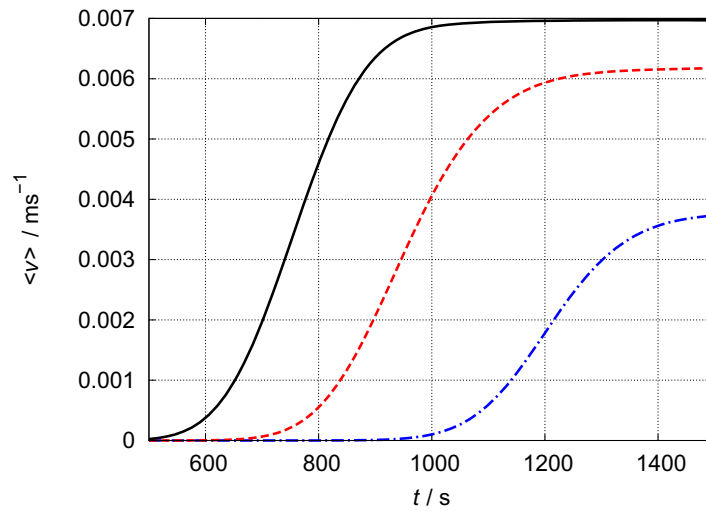


Figure 11. Development of the mean velocities of the TI as a function of time for different applied currents: $I = 14$ kA (blue line), $I = 16$ kA (red line) and $I = 18$ kA (black line).

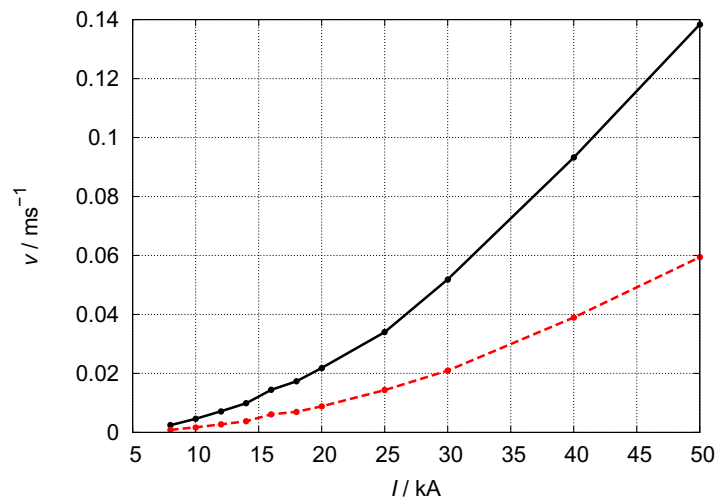


Figure 12. Dependence of velocity of the TI on the applied current I . The black line stands for maximum velocities and the red dashed line for averaged velocities.

long cuboid with a height of 1040 mm. For this case, we obtain $\lambda = 115$ mm, a value quite close to the corresponding value of the infinitely long cylinder.

Figure 13 shows now the critical currents as a function of height. In the limit of very tall cuboids, the critical current converges to a value of approximately 3 kA, which is also quite close to the value 2.7 kA for the infinitely long cylinder [19]. Shortening the cuboid, a first plateau of the critical current is observed at a height corresponding to the TI wavelength of 115 mm. Decreasing the height further, a sharp increase of the critical current is observed, which flattens again to a second plateau when the height comes close to the half wavelength (57.5 mm). Similar plateaus appear also in finite geometry Rayleigh–Bénard convection, see e.g. [32]. Shortening

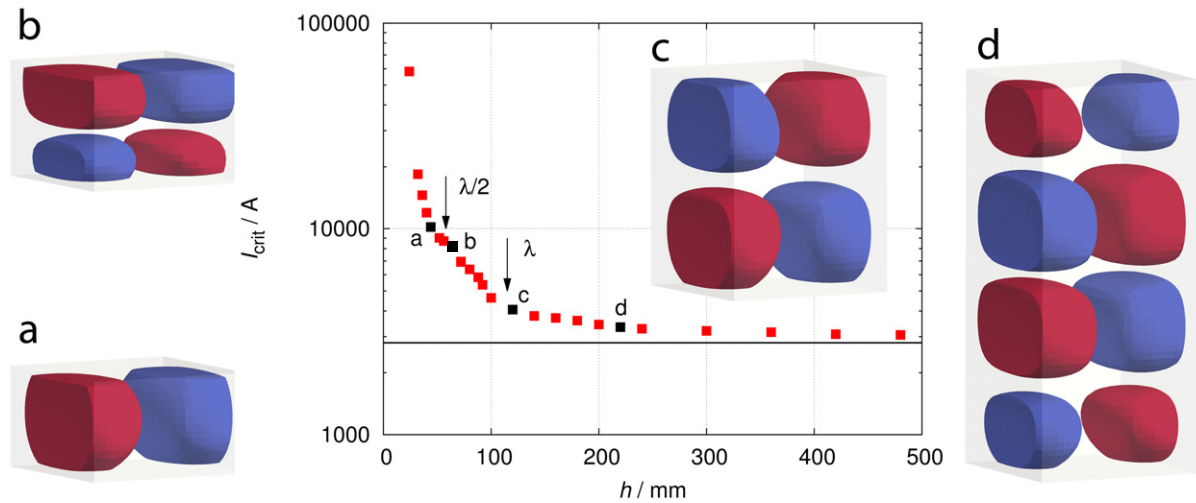


Figure 13. Dependence of the critical current for the onset of the TI on the height of a cuboid of $96 \times 96 \times h \text{ mm}^3$. If the height of the vessel drops below the wavelength of the TI, the critical current increases steeply. The black line marks the critical current for the infinite cylinder. The isosurface plots show the induced magnetic field b_z for four selected heights h , indicated by the black cubes in the graph. Below one half-wavelength ($h < \lambda/2$), only one convection cell is present (a). Slightly above $h = \lambda/2$, there are two cells (b). Panel (c) shows the case when $h = \lambda$. For $h = 1.9\lambda$ (d), we observe four cells, the top and bottom ones appearing somewhat smaller.

the cuboid still further, the critical currents rise extremely steeply. With regard to liquid metal batteries this would mean that very flat cells will not be affected by the TI.

For those heights which are below the half wavelength of the TI ($h < \lambda/2$), there is only one convection cell; for slightly taller vessels a second one appears (see figure 13, left). In general, the number of convection cells adapts to the height, and the cell size acquires a maximum if the height is a multiple of the wavelength. If h exceeds 1.5λ , a third cell may appear—but only in the case of a helical TI. In the case of non-helical TI an even number of convection cells seem to be more stable. Usually, the new convection cells appear at the top and/or bottom. If the height is slightly below an integer multiple of the characteristic wavelength, the upper and lower convection cells will appear somehow ‘compressed’ in comparison with the more central ones (figure 13, right).

5. Validation of experimental results

In a recent paper [1], we have evidenced the occurrence of the TI in a liquid metal experiment. A cylinder made of polyoxymethylene ($d = 100 \text{ mm}$, $h = 750 \text{ mm}$) was filled with the eutectic GaInSn, which is liquid at room temperature. A current of up to 8 kA was injected into the liquid metal through two massive copper electrodes at the top and bottom of the cylinder. In order to avoid any inhomogeneities of the electric current at the interface between Cu and GaInSn, we restrained from inserting ultrasonic transducers for the direct measurement of the velocity perturbations and relied exclusively on external measurements of the induced magnetic field.

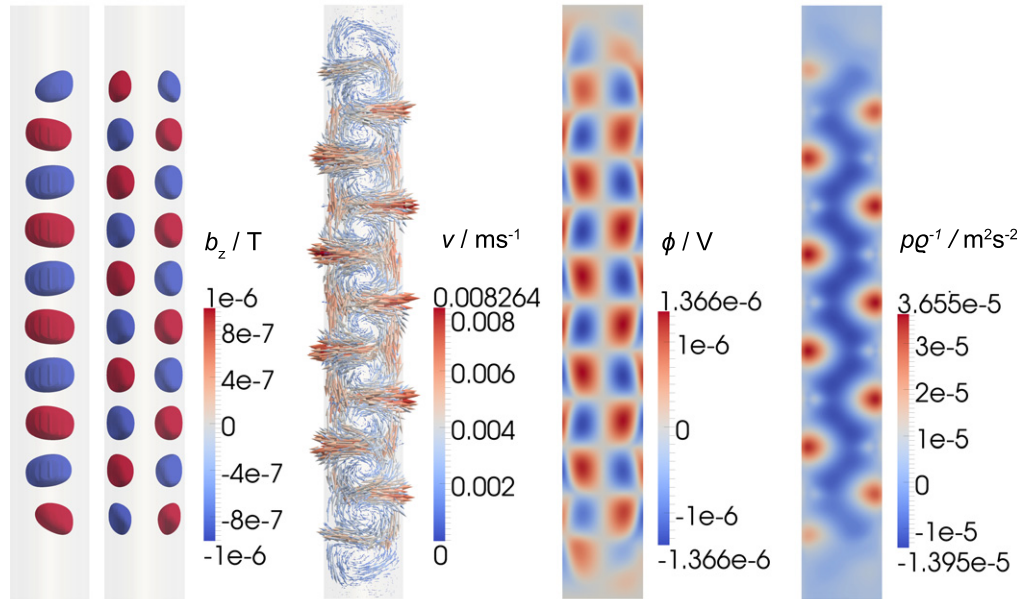


Figure 14. Iso-shapes for b_z (left), velocity field (second panel), electric potential (third panel) and pressure (right) of the saturated TI in a cylinder filled with GaInSn. The applied current is 10 kA. The magnetic field is shown in the x - and y -directions, and all other figures only in x .

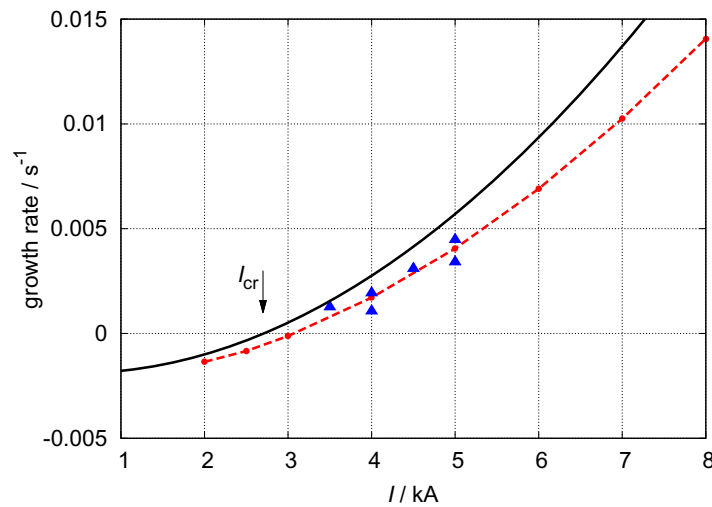


Figure 15. Growth rates of the TI in a cylinder filled with GaInSn. The black line marks the maximal possible growth rates for the infinite cylinder [19]. Our simulation (red dashed line) fits well the experimental data (blue triangles) [1].

The vertical component b_z was measured at 11 positions along the vertical axis of the device. With this setup, we were able to identify the growth rates of the short-wavelength perturbations due to the TI, before they gave way to a longer wavelength structure that we attributed to the thermal wind resulting from Joule heating in the GaInSn.

For this cylindrical geometry, we simulate the TI and compare the results with the available experimental data. The cylindrical fluid volume is meshed with a grid cell size of about

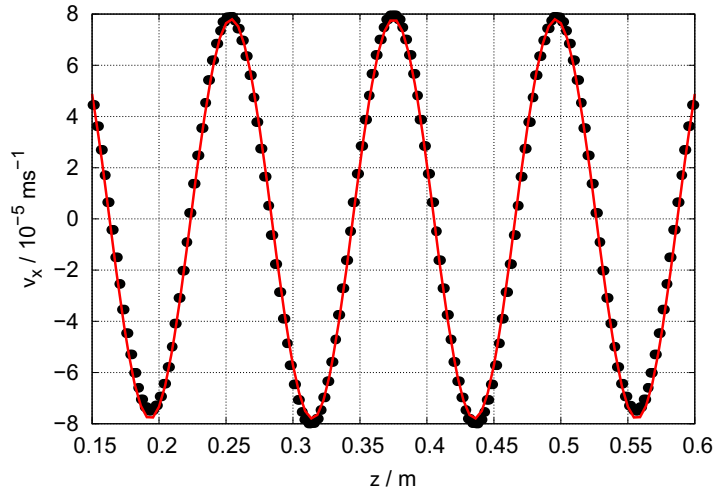


Figure 16. Velocities of the TI in the x -direction along the z -axis in the central part. Values are taken at the maximal growth rate, i.e. shortly before reaching saturation (black dotted line). The red fit allows one to determine the spatial wavelength of $\lambda = 121$ mm.

$3 \times 3 \times 3 \text{ mm}^3$. As the electrodes are relatively thick and are elongated by long power supply leads, we assume \mathbf{B}_0 to be constant over the height of the cylinder.

For an assumed current of 10 kA, the resulting convection cells of the TI are illustrated in figure 14. It should be noted that the number and shape of these convection cells are quite independent of the initial conditions.

In figure 15 the experimental growth rates are compared with the numerical ones. Simulations for the infinitely long cylinder [19] provide the maximum possible growth rates. As we do simulation for the real, i.e. finite cylinder, the resulting growth rates lie slightly below these values, but correspond nicely with the experimental data.

For our geometry the theoretical wavelength is $\lambda = 127$ mm [19]. This value matches the wavelength obtained by our finite length simulation (121 mm) fairly well, as inferred from figure 16.

6. Conclusion and outlook

On the basis of an integro-differential equation approach, we have developed a numerical tool that is particularly suited for investigations of current-driven magnetohydrodynamic instabilities in liquid metals. Employing the quasistatic approximation, the solution of the induction equation for the magnetic field was substituted by solving a Poisson equation for the induced current density, from which the magnetic field is computed via the Biot–Savart law. This procedure allows us to deal with instabilities in conducting fluids characterized by very small magnetic Prandtl numbers.

After examining the convergence properties of this numerical scheme, we have simulated the TI in different geometries, including cuboids and cylinders. For the cuboid it was shown in detail how the critical current increases with decreasing aspect ratio, exhibiting two remarkable plateaus at those heights corresponding to one or a half wavelength of the TI mode, respectively.

This curve may be directly used for defining a maximum aspect ratio of liquid metal batteries at a given charging current. Depending on the initial conditions our simulations have also shown the transient appearance of helical structures, i.e. the occurrence of chiral symmetry breaking.

For cylindrical geometry, we have numerically reproduced the growth rates of the TI that had been measured in a recent liquid metal experiment.

The main result of our simulations is that the saturation level of the TI-induced velocity for typical electrical currents is of the order of mm s^{-1} until cm s^{-1} . This is quite consistent with a formal scaling, by v/R , of the velocity levels as obtained at much larger magnetic Prandtl numbers [33]. While this good correspondence confirms the interaction parameter Ha^2/Re to be the governing parameter for the saturation over a wide range of magnetic Prandtl numbers, it makes physical interpretation of the saturation mechanism a bit more difficult. Actually, for Pm close to 1, Gellert *et al* [33] had identified a very plausible saturation mechanism in terms of a radially dependent increase of the TI-triggered turbulent resistivity (β effect) that modifies the radial current distribution in such a way as to make the magnetic field distribution just marginally stable. Evidently, this nice picture does not apply any more to small Pm , as considered here, since the velocity perturbations arising are much too weak to produce any noticeable turbulent resistivity. In this respect, a simple picture for understanding the saturation of TI at low Pm remains elusive.

In a next step, we plan to include in the numerical model the effects of thermal convection resulting from the Joule heating due to a strong current, which has turned out to be important in the experiment. We also develop a multiphase solver, which will allow us to simulate three-layer liquid metal batteries in detail.

On the experimental side, in the framework of the DRES-DYN project [34] we plan to set up a large-scale liquid sodium experiment for the combined investigation of the magneto-rotational instability, as recently investigated [35], and the TI.

Acknowledgments

This work was supported by Helmholtz-Gemeinschaft Deutscher Forschungszentren (HGF) in the framework of the ‘Initiative für mobile und stationäre Energiespeichersysteme’, and in the framework of the Helmholtz Alliance LIMTECH, as well as by Deutsche Forschungsgemeinschaft in the framework of the SPP 1488 (PlanetMag). We gratefully acknowledge fruitful discussions with Rainer Arlt, Alfio Bonanno, Marcus Gellert, Rainer Hollerbach, Jānis Priede, Günther Rüdiger and Martin Seilmayer on several aspects of the Tayler instability.

References

- [1] Seilmayer M, Stefani F, Gundrum T, Weier T, Gerbeth G, Gellert M and Rüdiger G 2012 *Phys. Rev. Lett.* **108** 244501
- [2] Tayler R J 1960 *Rev. Mod. Phys.* **32** 907–13
- [3] Bergerson W F, Forest C B, Fiksel G, Hannum D A, Kendrick R, Sarff J S and Stambler S 2006 *Phys. Rev. Lett.* **96** 015004
- [4] Vandakurov Y V 1972 *Astron. Zh.* **49** 324–33
- [5] Tayler R J 1973 *Mon. Not. R. Astron. Soc.* **161** 365–80
- [6] Spruit H C 2002 *Astron. Astrophys.* **381** 923–32

- [7] Zahn J P, Brun A S and Mathis S 2007 *Astron. Astrophys.* **474** 145–54
- [8] Suijs M P L, Langer N, Poelarends A J, Yoon S C, Heger A and Herwig F 2008 *Astron. Astrophys.* **481** L87–90
- [9] Yoon S C, Dierks A and Langer N 2012 *Astron. Astrophys.* **542** A113
- [10] Moll R, Spruit H C and Obergaulinger M 2008 *Astron. Astrophys.* **492** 621–30
- [11] Spies G O 1988 *Plasma Phys. Control. Fusion* **30** 1025–37
- [12] Cochran F L and Robson A E 1993 *Phys. Fluids B* **5** 2905–8
- [13] Rüdiger G, Schultz M and Gellert M 2011 *Astron. Nachr.* **10** 1–7
- [14] Huggins R E 2010 *Energy Storage* (New York: Springer Science/Business Media)
- [15] Bradwell D J, Kim H, Sirk A H C and Sadoway D R 2012 *J. Am. Chem. Soc.* **134** 1895–7
- [16] Weaver R D, Smith S W and Willmann N L 1962 *J. Electrochem. Soc.* **109** 653–7
- [17] Cairns E J and Shimotake H 1969 *Science* **164** 1347–55
- [18] Stefani F, Weier T, Gundrum T and Gerbeth G 2011 *Energ. Convers. Manage.* **52** 2982–6
- [19] Rüdiger G, Gellert M, Schultz M, Strassmeier K G, Stefani F, Gundrum T, Seilmayer M and Gerbeth G 2012 *Astrophys. J.* **755** 181
- [20] Davidson P A 2001 *An Introduction to Magnetohydrodynamics* (Cambridge: Cambridge University Press)
- [21] Meir A J, Schmidt P G, Bakhtiyarov S I and Overfelt R A 2004 *J. Appl. Mech.* **71** 786–95
- [22] OpenFOAM Foundation 2012 www.openfoam.org/
- [23] Gellert M, Rüdiger G and Hollerbach R 2011 *Mon. Not. R. Astron. Soc.* **414** 2696–701
- [24] Bonanno A, Brandenburg A, Del Sordo F and Mitra D 2012 *Phys. Rev. E* **86** 016313
- [25] Stefani F, Gerbeth G and Gailitis A 1999 Velocity profile optimization for the Riga dynamo experiment *Transfer Phenomena in Magnetohydrodynamics and Electroconducting Flows* ed A Alemany, P Marty and J P Thibault (Dordrecht: Kluwer) pp 31–44
- [26] Guermond J L, Laguerre R, Léorat J and Nore C 2007 *J. Comput. Phys.* **221** 349–69
- [27] Stefani F, Gerbeth G and Rädler K H 2000 *Astron. Nachr.* **321** 65–73
- [28] Iskakov A, Descombes S and Dormy E 2004 *J. Comput. Phys.* **197** 540–54
- [29] Giesecke A, Stefani F and Gerbeth G 2008 *Magnetohydrodynamics* **44** 237–52
- [30] Menter F 2002 *CFD Best Practice Guidelines for CFD Code Validation for Reactor-Safety Applications* (ECORA)
- [31] Faires J D and Burden R L 2003 *Numerical Methods* (Pacific Grove, CA: Brooks Cole)
- [32] Gelfgat A Y 1999 *J. Comput. Phys.* **156** 300–24
- [33] Gellert M and Rüdiger G 2009 *Phys. Rev. E* **80** 046314
- [34] Stefani F, Eckert S, Gerbeth G, Giesecke A, Gundrum T, Steglich C, Weier T and Wustmann B 2012 *Magnetohydrodynamics* **48** 103–13
- [35] Stefani F, Gerbeth G, Gundrum T, Hollerbach R, Priede J, Rüdiger G and Szklarski J 2009 *Phys. Rev. E* **80** 066303